

---

## **Rapid inversion of data from 2-D resistivity surveys with electrodes displacements**

M.H. Loke<sup>1\*</sup>, P.B. Wilkinson<sup>2</sup>, J. E. Chambers<sup>2</sup> and P.I. Meldrum<sup>2</sup>

<sup>1</sup> Geotomosoft Solutions, 115 Cangkat Minden Jalan 6, 11700 Gelugor, Penang, Malaysia.

email : drmhloke@yahoo.com

<sup>2</sup> British Geological Survey, Environmental Science Centre, Keyworth, Nottingham, NG12 5GG, UK

email : pbw@bgs.ac.uk, jecha@bgs.ac.uk, pime@bgs.ac.uk

\* Corresponding author

## **ABSTRACT**

Resistivity monitoring surveys are used to detect temporal changes in the subsurface using repeated measurements over the same site. The positions of the electrodes are typically measured at the start of the survey program and possibly at occasional later times. In areas with unstable ground, such as landslide prone slopes, the positions of the electrodes can be displaced by ground movements. If this occurs at times when the positions of the electrodes are not directly measured, they have to be estimated. This can be done by interpolation or, as in recent developments, from the resistivity data using new inverse methods. The smoothness-constrained least-squares optimisation method can be modified to include the electrode positions as additional unknown parameters. The Jacobian matrices with the sensitivity of the apparent resistivity measurements to changes in the electrode positions are then required by the optimisation method. In this paper, a fast adjoint-equation method is used to calculate the Jacobian matrices required by the least-squares method to reduce the calculation time. In areas with large near-surface resistivity contrasts, the inversion routine sometimes cannot accurately distinguish between electrodes displacements and subsurface resistivity variations. To overcome this problem, the model for the initial time-lapse data set (with accurately known electrode positions) is used as the starting model for the inversion of the later-time data set. This greatly improves the accuracy of the estimated electrode positions compared to the use of a homogeneous half-space starting model. In areas where the movement of the electrodes is expected to occur in a fixed direction, the method of transformations can be used to include this information as an additional constraint in the optimisation routine.

**Keywords :** Resistivity, Time lapse, Imaging, Inversion, Monitoring

## INTRODUCTION

The past two decades have seen a rapid expansion in the use of two-dimensional (2-D) resistivity surveys. They have been used for a wide range of applications ranging from archaeological, hydrological, geotechnical, environmental and mineral exploration problems (Auken *et al.* 2006; Loke *et al.* 2013). In recent years, there has been increasing interest in geoelectrical monitoring surveys to detect temporal changes in the subsurface (Chambers *et al.* 2014; Supper *et al.* 2014a). One such application is the monitoring of potentially unstable slopes (Chambers *et al.* 2011; Gunn *et al.* 2013; Supper *et al.* 2014b; Chambers *et al.* 2014; Uhlemann *et al.* 2015a). These monitoring measurements are frequently carried out over several months or even years. The positions of the electrodes are measured at the start of the campaign and usually also at regular intervals (e.g. Uhlemann *et al.* (2015a)). However, movements of the ground sometimes occur between periods of electrode position measurements. Consequently, the precise positions of the electrodes might not be accurately known for some data sets.

Therefore the inverse problem on unstable ground is not only to determine the subsurface resistivity, but also to determine the positions of the electrodes that have shifted from the last known locations. Wilkinson *et al.* (2010; 2015a; 2016) proposed using the changes in the apparent resistivity, for data acquired from a time-lapse survey, to estimate the changes in the electrode positions. An innovative approach for 2-D resistivity surveys was presented by Kim (2014) where the least-squares optimisation method was modified to include both the subsurface resistivity and electrode positions as unknown variables to be determined. The perturbation method (McGillivray and Oldenburg 1990) was used to estimate the required Jacobian matrix of partial derivatives. In this paper we present a computationally more efficient method to determine Jacobian matrix. We also propose a

modification of the inversion algorithm that uses the inversion model from a previous time-lapse data set as a constraint.

In the next section, we briefly describe the smoothness-constrained least-squares optimisation method and the modifications made to include the electrode positions as unknown parameters. This is followed by a description of a modification to the adjoint-equation method (McGillivray and Oldenburg 1990) to calculate the required Jacobian matrices. Previous work by Kim (2014) showed that subsurface resistivity variations can be mistakenly modelled as changes in the electrode positions. We describe a modified inversion algorithm that uses the model from a previous time-lapse data set (with accurately known electrode positions) as a constraint to reduce this artefact. We then present examples of inversions of synthetic and field data sets from an active landslide using the modified inversion algorithm.

## THEORY

### The constrained least-squares optimisation method

The smoothness-constrained least-squares optimisation method is frequently used for 2-D and 3-D inversion of resistivity data (deGroot-Hedlin and Constable 1990; Sasaki 1989, 1994; Loke, Acworth and Dahlin 2003). The optimisation equation that gives the relationship between the model parameters and the measured data (Farquharson and Oldenburg 1998) is :

$$\left[ \mathbf{J}_{i-1}^T \mathbf{R}_d \mathbf{J}_{i-1} + \lambda_i^2 (\mathbf{W}^T \mathbf{R}_m \mathbf{W} + \delta \mathbf{I}) \right] \Delta \mathbf{r}_i = \mathbf{J}_{i-1}^T \mathbf{R}_d \mathbf{g}_{i-1} - \lambda_i^2 (\mathbf{W}^T \mathbf{R}_m \mathbf{W} + \delta \mathbf{I}) (\mathbf{r}_{i-1} - \mathbf{r}_0). \quad (1)$$

In equation (1), the Jacobian matrix  $\mathbf{J}$  contains the partial derivatives of the (logarithm of the) apparent resistivity values with respect to the (logarithm of the) model resistivity values.  $\lambda$  is the damping factor and  $\mathbf{g}$  is the data misfit vector.  $\mathbf{r}_{i-1}$  is the model parameters

vector for the previous iteration, while  $\Delta \mathbf{r}_i$  is the change in the model parameters.  $\mathbf{W}$  incorporates the roughness filters in the  $x$ - and  $z$ -directions.  $\mathbf{R}_d$  and  $\mathbf{R}_m$  are weighting matrices introduced so that different elements of the data misfit and model roughness vectors are given equal weights if the L1-norm inversion method is used (Farquharson and Oldenburg 1998; Loke *et al.* 2003). In this equation, we also apply a reference background homogenous model  $\mathbf{r}_0$  with all resistivity values equal to the average apparent resistivity. The associated damping factor  $\delta$  is usually set at a small but non-zero value (Oldenburg and Li Y. 1994; Li and Oldenburg 2000). It prevents the components of the  $\Delta \mathbf{r}_i$  vector having excessively large amplitudes if the data is very noisy. We use a value of 0.01 for  $\delta$ .

The model parameters vector has the following form for a model with  $m$  cells.

$$\mathbf{r} = \begin{pmatrix} r_1 \\ r_2 \\ \cdot \\ \cdot \\ r_m \end{pmatrix}, \quad (2)$$

where  $r_j$  represents the logarithm of the resistivity of the  $j$ th model cell. To include the positions of the electrodes as additional unknown parameters, the extended model parameters vector  $\mathbf{q}$  for a survey line with  $e$  electrodes has the following form.

$$\mathbf{q} = \begin{pmatrix} r_1 \\ \cdot \\ r_m \\ x_2 \\ \cdot \\ x_e \\ z_2 \\ \cdot \\ z_e \end{pmatrix} = \begin{pmatrix} \mathbf{r} \\ \mathbf{x} \\ \mathbf{z} \end{pmatrix} \quad (3)$$

We note that the apparent resistivity values only depend on the relative positions of the electrodes. The first electrode at  $(x_1, z_1)$  is used as a reference point, and the shifts of the other



When this is applied to the  $(\mathbf{x}_i - \mathbf{x}_0)$  vector, this minimises differences (in both the amplitude and direction) in the horizontal shifts between neighbouring electrodes. As an example, on a downhill slope, if an electrode moves down the slope (such as in the  $-x$  direction), normally we would expect the neighbouring electrode to move in the same direction (i.e. also in the  $-x$  direction).  $\alpha$  and  $\gamma$  are the relative weights given to the damping factor applied to the horizontal and vertical shifts in the electrode positions.

A final modification is required in the second term on the right hand side of equation (1). This term applies the roughness filter to the model resistivity values  $\mathbf{r}_{i-1}$  obtained from the previous iteration. This ensures that the model resistivity has minimal roughness (Farquharson and Oldenburg 1998). In a survey, we assume that the initial horizontal and vertical positions of the electrodes  $(\mathbf{x}_0, \mathbf{z}_0)$  are accurately known and the shifts in the positions of the electrodes are less than the spacing between the electrodes. We thus attempt to minimise the shifts in the calculated electrode positions from the original known positions in the following equation.

$$\mathbf{q}_{i-1} = \begin{pmatrix} \mathbf{r}_{i-1} - \mathbf{r}_0 \\ \mathbf{x}_{i-1} - \mathbf{x}_0 \\ \mathbf{z}_{i-1} - \mathbf{z}_0 \end{pmatrix} \quad (7)$$

The final modified smoothness-constrained least-squares equation is as follows.

$$\left[ \mathbf{G}_{i-1}^T \mathbf{R}_d \mathbf{G}_{i-1} + \lambda_i^2 (\mathbf{V}^T \mathbf{R}_m \mathbf{V} + \delta \mathbf{I}) \right] \Delta \mathbf{q}_i = \mathbf{G}_{i-1}^T \mathbf{R}_d \mathbf{g}_{i-1} - \lambda_i^2 (\mathbf{V}^T \mathbf{R}_m \mathbf{V} + \delta \mathbf{I}) \mathbf{V}^T \mathbf{R}_m \mathbf{V} \mathbf{q}_{i-1} \quad (8)$$

The above formulation is slightly different from that used by Kim (2014) in that it includes the second term on the right-hand side that ensures the model resistivity and changes in the electrode positions vary in a smooth manner.

A homogeneous half-space is commonly used as the starting model (Loke and Barker 1996) for the optimisation algorithm. The problem of shifts in electrode positions can frequently occur during a series of measurements in a time-lapse survey when, for example,



monitoring an active landslide (Wilkinson *et al.* 2016). The initial positions of the electrodes are usually accurately measured and can be considered as fixed parameters in the inversion of the initial data set. Frequently temporal changes in the subsurface resistivities are usually much smaller than spatial variations (Loke, Dahlin and Rucker 2014). Thus, the resistivity model obtained from the inversion of the initial data set should provide a good starting model for the later time data sets. The initial data misfit would then be largely due to changes in the positions of the electrodes. This should help in differentiating changes in the apparent resistivity due to shifts in the electrode positions and those due to spatial variations in the subsurface resistivity. We therefore also test a modification of the inversion algorithm that uses the results of the initial survey as the starting model.

#### **A fast method to calculate the Jacobian matrix**

The finite-element method is commonly used to calculate the apparent resistivity values for surveys over areas with topography (Loke 2000). The potentials are calculated by solving the following capacitance matrix equation (Sasaki 1989; Silvester and Ferrari 1990).

$$\mathbf{C}\Phi = \mathbf{s} \tag{9}$$

$\Phi$  is a vector that contains the potentials at the nodes of the finite-element grid while  $\mathbf{s}$  is the current source vector.  $\mathbf{C}$  is the capacitance matrix that contains the positions of the nodes and the model conductivity values. The capacitance matrix is a positive definite symmetric sparse matrix (Silvester and Ferrari 1990). For 2-D models, a direct method such as the band Cholesky decomposition method is commonly used to solve this equation (Schwartz, Rutishauser and Stiefel 1973; Dey and Morrison 1979; Jennings and McKeown 1992). If 2-D finite-element linear quadrilateral elements (Figures 1a,1b) are used, it has 9 non-zero sub-diagonals (Figure 1c). In the least-squares inversion method, it is necessary to calculate the change in the potentials due to a change in the resistivity of each model cell  $r_j$  (or

equivalently the conductivity  $\sigma_j$ ). A simple but relatively inefficient method is the perturbation method (McGillivray and Oldenburg 1990) using a one-sided finite-difference formula, such as

$$\frac{\partial \phi_i}{\partial \sigma_j} \approx \frac{\phi_i(\sigma + \Delta \sigma_j) - \phi_i(\sigma)}{\Delta \sigma_j}. \quad (10)$$

In practice, this method is not used as it requires a new solution of equation (9) for each model parameter. A more commonly used method is the adjoint-equation approach (Sasaki 1989; McGillivray and Oldenburg 1990). Differentiating the capacitance matrix equation (9) with respect to the model cell conductivity  $\sigma_j$  leads to the following relationship.

$$\mathbf{C} \frac{\partial \Phi}{\partial \sigma_j} = \mathbf{s}', \text{ where } \mathbf{s}' = -\frac{\partial \mathbf{C}}{\partial \sigma_j} \Phi \quad (11)$$

This has the same form as equation (9), except the current source vector  $\mathbf{s}$  is replaced by a vector  $\mathbf{s}'$  formed by the multiplication of the  $\frac{\partial \mathbf{C}}{\partial \sigma_j}$  matrix and the potential vector  $\Phi$  (due to

the source  $\mathbf{s}$ ). All the information required to calculate  $\frac{\partial \Phi}{\partial \sigma_j}$  is available in the process of

solving equation (9) to calculate the potentials. The matrix  $\frac{\partial \mathbf{C}}{\partial \sigma_j}$  is very sparse with only 16

non-zero terms for a 2-D linear quadrilateral element. The terms in the capacitance matrix  $\mathbf{C}$  consist of the coupling coefficients between the nodes in each element in the finite-element mesh (Silvester and Ferrari 1990) and the conductivity of the element. The coupling coefficient between two nodes in an element (Figure 1a) has the following form.

$$c_{pq} = k_{pq}(x, z) \sigma_j \quad (12)$$

The function  $k_{pq}(x, z)$  depends only on the coordinates of the four nodes at the corners of the quadrilateral element. The derivative of the coupling coefficient with respect to the element conductivity is thus given by

$$\frac{\partial c_{pq}}{\partial \sigma_j} = k_{pq}(x, z). \quad (13)$$

As the  $k_{pq}(x, z)$  terms are calculated in the process of constructing the capacitance matrix  $\mathbf{C}$  in equation (9), it is not necessary to recalculate them for  $\frac{\partial \mathbf{C}}{\partial \sigma_j}$  matrix.

In the adjoint-equation method, for a survey line with  $e$  electrodes we first calculate the potential vectors ( $\Phi_1, \Phi_2, \dots, \Phi_e$ ) due to a single current electrode at each electrode position. Consider the simple case where the measurement was made using a current electrode at position 1 and a potential electrode at 2. We first calculate the matrix vector product  $\frac{\partial \mathbf{C}}{\partial \sigma_j} \Phi_1$ . If  $\sigma_j$  is the conductivity of a quadrilateral mesh element (such as in Figure 1a), the  $\frac{\partial \mathbf{C}}{\partial \sigma_j}$  matrix has a total of 16 non-zero elements distributed along 4 rows

corresponding to the 4 nodes of the quadrilateral. Multiplication of the  $\frac{\partial \mathbf{C}}{\partial \sigma_j}$  matrix with the

$\Phi_1$  vector gives a vector  $\mathbf{s}'_{12}$  with four non-zero elements corresponding to the nodes at the corners of the element. The  $\frac{\partial \Phi}{\partial \sigma_j}$  vector can then be calculated by adding the potentials at

electrode 2 due to four "fictitious" current sources located at the corners of the mesh element.

From the principle of reciprocity, the potential due to a current source at a mesh node (for example node 3 in Figure 1a) at electrode 2, is the same as the potential at the node due to a

current source at electrode 2. Thus the  $\frac{\partial \Phi}{\partial \sigma_j}$  vector for a measurement with electrodes 1 and 2

is calculated from a weighted sum of the potential vector  $\Phi_2$ , with the weights given by the

$\frac{\partial \mathbf{C}}{\partial \sigma_j} \Phi_1$  matrix vector product. The Jacobian matrix values for a general array with four

electrodes can be easily calculated by using the net potentials of the current and potential

dipoles. For example, if the array has the current electrodes at positions 1 and 4 and the potential electrodes at 2 and 3, we use the  $(\Phi_1 - \Phi_4)$  and  $(\Phi_2 - \Phi_3)$  vectors in the calculations.

Bing and Greenhalgh (1999) presented an alternative method of calculating the Jacobian matrix based on the use of Green's function. Instead of using the derivative of the capacitance matrix, the matrix terms are calculated from the potentials at the nodes of the element. However, the number of numerical operations needed to calculate the Jacobian matrix values is similar to the adjoint-equation approach.

Kim (2014) used the perturbation method to calculate the necessary partial derivatives due to changes in the electrode positions. For example, consider a change in the  $z$ -position of electrode number 2. This is approximated by

$$\frac{\partial \phi_i}{\partial z_2} \approx \frac{\phi_i(z_2 + \Delta z_2) - \phi_i(z_2)}{\Delta z_2}. \quad (14)$$

For a survey line with  $e$  electrodes, and assuming the first electrode is kept fixed, it will be necessary to recalculate the potentials  $2(e-1)$  times for 2-D problems. While this is possible for 2-D problems, it is inefficient and would not be practical for future extensions to 3-D inversions (Loke, Wilkinson and Chambers 2016). Instead, we describe a modification of the adjoint-equation approach to calculate the  $\mathbf{X}$  and  $\mathbf{Z}$  Jacobian matrices in equation (4). As an example, the change in the potential values due to a shift in the  $z$  direction for the  $k$ th electrode can be obtained by differentiating the capacitance matrix equation (9) with respect to  $z_k$ . This gives the following equation.

$$\mathbf{C} \frac{\partial \Phi}{\partial z_k} = - \frac{\partial \mathbf{C}}{\partial z_k} \Phi \quad (15)$$

The problem then becomes one of calculating the necessary non-zero terms in the  $\frac{\partial \mathbf{C}}{\partial z_k}$  matrix. Figure 2 shows part of the 2-D mesh used by the finite-element routine with 4 nodes (i.e. 4 cells) between adjacent electrodes. A shift in the position of one electrode (such

as electrode 3) will only affect the nodes that lie between that electrode and adjacent electrodes (i.e. electrodes 2 to 4). Thus the  $\frac{\partial \mathbf{C}}{\partial z_k}$  matrix will have a relatively small number of non-zero terms compared to the full  $\mathbf{C}$  matrix (Figure 1c). The change in the coupling coefficients can be calculated analytically or numerically. For convenience, we calculate it numerically using a two-sided difference formula as follows.

$$\frac{\partial c_{pq}}{\partial z_k} \approx \frac{k_{pq}(x, z_k + \Delta z_k) - k_{pq}(x, z_k - \Delta z_k)}{2\Delta z_k} \sigma_j \quad (16)$$

The use of a two-sided formula avoids any possible directional bias that might be present in a one-sided formula such as in (14). The time required to calculate the  $k_{pq}(x, z)$  terms is negligible compared to resolving equation (9) as required by the perturbation method. After calculating the non-zero elements of the  $\frac{\partial \mathbf{C}}{\partial z_k}$  matrix, the change in the partial

derivative vector  $\frac{\partial \Phi}{\partial z_k}$  values can be calculated in a similar way as for the  $\frac{\partial \Phi}{\partial \sigma_j}$  vectors by using the potentials at the nodes due to current sources at the current and potential dipoles.

If the 2-D finite-element mesh has  $n_z$  nodes in the vertical direction, the number of mesh nodes affected by a shift at an electrode is  $7n_z$  if there are 3 nodes (4 cells) between adjacent electrodes. As the maximum number of non-zero values in each row of the capacitance matrix is 9 (Figure 1c), the number of multiply-add operations need to calculate the Jacobian value for an electrode shift (in the  $x$  or  $z$  direction) is then  $70n_z$  for one data point per electrode. The total number of operations needed to calculate both the  $\mathbf{X}$  and  $\mathbf{Z}$  matrices for a survey with  $d$  data points and  $e$  electrodes is then  $140n_z d(e-1)$ . As an example, to illustrate the relative computational requirements of the adjoint-equation and perturbation methods, we use a dipole-dipole survey described by Seaton and Burbey (2000) that has 469 data points using a line with 50 electrodes. A typical finite-element mesh used for the

inversion of the survey line has 237 nodes in the  $x$ -direction ( $n_x$ ) and 34 nodes in the  $z$ -direction ( $n_z$ ). The adjoint-equation method requires about  $1.1 \times 10^8$  numerical operations to calculate the  $\mathbf{X}$  and  $\mathbf{Z}$  Jacobian matrices. The band method that is used to solve the capacitance matrix equation (Dey and Morrison 1979) requires about  $0.5n_x n_z (n_z + 1)(n_z + 4)$  multiply-add operations for the factorisation step and  $4(e - 1)n_x n_z (n_z + 2)$  operations for the solution step (Schwartz *et al.* 1973; Jennings and McKeown 1992; Golub van Loan 1996) to calculate the required potentials for the  $x$  or  $z$  shifts of the electrodes. For this survey line, the perturbation method would require about  $6.2 \times 10^9$  numerical operations which is about 56 times greater than the adjoint-equation method.

We note that for 2-D models with a point (3-D) current source, a Fourier transform of the associated partial differential equation is usually carried out (Dey and Morrison 1979; Queralt, Pous and Marcuello 1991; Xu, Duan and Zhang 2000). Calculation of the potentials involve solving the capacitance matrix equation a number (usually 4 to 12) times for different wave-number values. However, the relative efficiencies of the perturbation and adjoint-equation methods are still the same as the same numerical operations are carried out for each wave-number value.

## RESULTS

### Effect of shifts in the electrode positions

In this section, we examine the effect of shifts in the  $x$  and  $z$  directions of electrodes in a 2-D survey. To simplify the comparisons, we use a homogenous half-space of  $100 \Omega\text{m}$  as the background medium. Accordingly, the measured apparent resistivity values should also be  $100 \Omega\text{m}$  in the unperturbed setup. The finite-element routine used (Queralt *et al.* 1991) gives an average error of about 1% in the calculated apparent resistivity values. Figure 3

shows the apparent resistivity pseudosections for the dipole-dipole array (with  $a=1$  m and  $n=1$  to 10) obtained after shifting the electrode at the 10 m mark by 0.1 m in a survey line with 21 electrodes 1 m apart. The apparent resistivities are calculated using the geometric factors based on the assumption the electrodes are uniformly spaced (i.e. there was no shift). A horizontal shift (Figure 3a) has a larger effect compared to an upwards or downwards vertical shift (Figures 3b and 3c). The horizontal shift results in apparent resistivity values of 81 to 127  $\Omega\text{m}$  for the dipole-dipole array. In comparison, the upwards vertical shift gives a range of 95 to 110  $\Omega\text{m}$  and the downwards shift gives a range of 90 to 105  $\Omega\text{m}$ . In general, the effect of a horizontal shift is about 3 times larger than a vertical shift of the same magnitude (Table 1). We also examine the effect of  $\pm 10\%$  changes in the resistivity of a 1 m<sup>2</sup> block of the subsurface directly below the electrode at the 10 m mark (Figures 3d and 3e).

The rightwards horizontal shift reduces the distances between the shifted electrode and those on the right which increases the potential values (and consequently the calculated apparent resistivity using the geometric factors for equally spaced electrodes). Similarly, the increase in the distance from the electrodes to the left reduces the apparent resistivity on the left side of the dipole-dipole array pseudosection. The horizontal shift only affects array measurements that involve the shifted electrode.

A vertical shift also affects measurements that do not involve the shifted electrode if it lies between the electrodes in the array used (due to the change in the immediate topography). We also note that an upwards vertical shift tends to increase the apparent resistivity values directly below the electrode position with two low resistivity 'wings' on both sides (Figure 3c). A downwards shift produces the opposite pattern (Figure 3c). An increase in the subsurface block resistivity generally increases the apparent resistivity (Figure 3d) measured directly above the block. This is similar to an upwards shift although the pattern depends on the array type used and the depth of the block.

## 2-D synthetic model

Figure 4 shows the 2-D synthetic test model used. Figure 4a shows the model below a survey line with 31 electrodes with a uniform spacing of 1 m on a flat surface. It has a high resistivity prism (500  $\Omega\text{m}$  with depth to top of 1.0 m) and a slightly deeper low resistivity prism (20  $\Omega\text{m}$  with depth to top of 1.55 m) embedded in a 100  $\Omega\text{m}$  uniform medium. Figure 4b shows the perturbed model with four changes made. The electrode at the 5.0 m mark is shifted 0.3 m to the right while the electrodes at the 4.0 and 6.0 m marks are not moved. The electrode at the 17.0 m mark is shifted 0.4 m. upwards. In addition, a small resistivity change near the surface is introduced by adding a prism of 70  $\Omega\text{m}$  (with depth of 1.0 m to the top) between the two prisms. Finally, the base of the 20  $\Omega\text{m}$  low resistivity prism is extended downwards by 0.73 m. The measured data consists of dipole-dipole arrays with the '*a*' dipole length ranging from 1 to 4 m, and the '*n*' dipole separation factor ranging from 1 to 6. This gives a total of 415 data points. Voltage dependent Gaussian random noise (Zhou and Dahlin 2003) with a mean amplitude of 2.5 m $\Omega$  was added to the data before they were converted to apparent resistivity values. The measurements have resistance values ranging from 22 to 10491 m $\Omega$ . The added noise has a maximum amplitude of about 11% for the measurements with the lowest resistance values. The average noise level for the entire data set when converted to apparent resistivity is about 1.0%.

We first carry out an inversion of the initial and perturbed data sets assuming that the electrodes are equally spaced with no topography. The number of cells (*m*) used in the inversion model is 300. We use the 'discrepancy method' to select the appropriate damping factor (Farquharson and Oldenburg 2004) that gives a data misfit close to the known noise level. We also use the L1-norm (Farquharson and Oldenburg 1998; Loke *et al.* 2003) for both the data misfit and model roughness. The model for the initial data set is close to the true model (Figure 4a) with a data misfit of 1.0%. However, the inversion of the perturbed data



set failed to converge. We show the results after 6 iterations with a data misfit of 1.4% where the least-squares optimisation routine becomes trapped in a local minimum (Press *et al.* 1992). Further iterations reduced the data misfit by less than 0.1% at the expense of extreme model resistivity values ranging from less than 10  $\Omega\text{m}$  to more than 1000  $\Omega\text{m}$ . There are near-surface artefacts at the positions of the two electrodes at the 5 and 17 m marks that were shifted from the original positions. The horizontal shift at the 5 m mark produces alternating low and high resistivity near-surface variations. The anomaly corresponding to the low resistivity prism located between the 7 and 9 m marks is also distorted. The effect of the upwards shift at the 17 m mark is relatively small compared to the horizontal shift. It produces a small low resistivity artefact near the surface and higher resistivity values near the base of the model (Figure 4b). Note that the high resistivity prism, which is located further away from the shifted electrodes, is relatively well resolved.

The inclusion of the electrode positions as variables introduces new damping factor terms in equation (5) that makes the determination of the optimal damping factors for the three sets of parameters ( $\lambda$ ,  $\alpha$  and  $\gamma$ ) a more complex problem. The relative damping factors  $\alpha$  and  $\gamma$  (for  $x$  and  $z$  movements of the electrodes) are set to the same value in the following tests. We carry out tests using values ranging from 1 to 50 for  $\alpha$  and  $\gamma$ . In the initial set of tests, we use a homogeneous half-space (the average apparent resistivity value) as the initial model for the optimisation routine, and vary both the subsurface resistivity and electrode positions to reduce the data misfit. The L1-norm method was also used for the  $\mathbf{W}_x$  and  $\mathbf{W}_z$  roughness filters. The resulting inverse models, including the surface topography from the calculated positions of the electrodes, are shown in Figure 5. The three subsurface prisms are relatively well resolved. In particular, the two low resistivity prisms do not show the distortions observed when the electrode positions were fixed (Figure 4b). The upwards spike in the elevation of the electrode at the 17 m mark is clearly shown. However, there are

distortions in the surface profile over the high resistivity prism particularly when a small relative damping factor of 1 is used (Figure 5a). This is more clearly shown in the profile plots in Figure 6a where a vertical exaggeration of 10 is used for the elevation axis. The inversion algorithm is not able to fully distinguish between the effects of vertical shifts in the electrodes and an increase in the shallow subsurface resistivity. The anomaly patterns due to a vertical shift (Figure 3b) and a shallow high resistivity prism (Figure 3d) have similar patterns. The artefact in the vertical position of the surface profile is progressively reduced when the damping factor is increased. It is almost completely eliminated when a relative damping factor of 10 is used. However, the use of a higher damping factor also decreases the spike in the elevation at the electrode located at the 17 m mark (Figure 6a). Using a high damping factor of 50 essentially fixes the electrode positions (Figure 5f) giving a model similar to that with fixed electrodes (Figure 4b).

To numerically assess the accuracy of the inversion routine we calculate the difference in the positions of the electrodes calculated  $(x_c, z_c)$  from the inversion routine and the true  $(x_t, z_t)$  positions. The normalized error in the position of an electrode ( $s$ ) is calculated using the following formula.

$$s = \left[ (x_t - x_c)^2 + (z_t - z_c)^2 \right]^{0.5} / u \quad (17)$$

$u$  is the unit electrode spacing which is 1 m in this example. We use the normalized error as it is a dimensionless quantity. We then calculate the root-mean-squared (RMS) deviation for all the electrodes.

$$S_r = \left[ \frac{1}{m} \sum_{i=1}^{n_e} s_i^2 \right]^{0.5} \quad (18)$$

Another criterion used is the RMS difference between the logarithms of the calculated  $(\rho_c)$  and true model  $(\rho_t)$  resistivity values using the following equation.

$$R_r = \left[ \frac{1}{m} \sum_{i=1}^m (\log(\rho_{ii}) - \log(\rho_{ci}))^2 \right]^{0.5} = \left[ \frac{1}{m} \sum_{i=1}^m (\log(\rho_{ii} / \rho_{ci}))^2 \right]^{0.5} \quad (19)$$

Note that  $R_r$  is also a dimensionless quantity.

Changing the relative damping factor does not have a significant effect on the data misfit for values of 1 to 10 which remains at about 1.0% (Table 2). There is a slight increase in the data misfit with a damping factor ( $\alpha$ ) of 20 and a significant increase to 1.3% with a value of 50. Using a relative damping factor of 1 gave the largest RMS electrode positions misfit  $S_r$ . The large electrode positions misfit is due to the distortions in the surface profile caused by the subsurface resistivity variations (Figure 5a). Using a value of 20 for  $\alpha$  gives the lowest value for the RMS positions misfits  $S_r$  but it has a slightly higher data misfit of 1.1% and significant distortions in the resistivity model near the 5 m mark (Figure 5e). The optimum value of  $\alpha$  is probably between 3 and 10. The model resistivity misfit ( $R_r$ ) shows a smaller variation for values of 1 to 10 for  $\alpha$ . To reduce the statistics to a single number ( $S_A$ ), we calculate the combined positions and resistivity misfits,  $S_A = S_r + R_r$ . The relative damping factor that gives the lowest combined misfit is 10.

The problem of displacements in the electrode positions usually occurs in the context of a time-lapse survey. In the initial survey setup, the positions of the electrodes are typically accurately measured, and thus can be considered to be known for the initial data set. Thus, the initial inverse model is a good estimate of the true subsurface resistivity. This provides an additional constraint that can be used to reduce the ambiguity in the inversion of later time data sets where the electrode positions are treated as unknown variables. We modify the inversion algorithm where the model obtained from the inversion of the initial time lapse data set (Figure 4a) is used as the starting model for the inversion of a later time data set. If the same array configurations are used for both surveys, the initial data misfit is essentially the difference between the apparent resistivity values of the two data sets. Wilkinson *et al.* (2010;

2015a; 2016) in fact used this difference to estimate the change in the electrode positions using the Jacobian matrix values of a homogenous half-space. Using the model from the initial data set as the initial model for the inversion of a later time data set effectively removes the effect of the common background resistivity structures. This method has the advantage that it can also be used when different array configurations are used for the two data sets (Wilkinson *et al.* 2015b). Figure 7 shows the resulting inversion models using this technique. The distortions in the surface profile over the high resistivity block are greatly reduced even when the smallest relative damping factor ( $\alpha$ ) of 1 is used (Figure 7a). This is more clearly shown in the profile plots in Figure 6b. Using a value of 1 for  $\alpha$  gives the lowest overall position misfit ( $S_r$ ). The lowest resistivity model misfit ( $R_r$ ) is obtained with values of 3 and 6 for  $\alpha$  (Table 2). Thus, the optimum value for  $\alpha$  is probably between 1 and 6.

### **Field data set from an active landslide**

The field data comes from the active Hollin Hill landslide, located near Malton, U.K., where an automated geoelectrical monitoring system has been making measurements on alternating days since March 2008 (Wilkinson *et al.* 2010). The site is a slow to very slow moving multiple earth slide-earth flow on a south-facing hill with a mean slope of  $14^\circ$ . From the base to the top of the slope, the formations are the Lias Group Redcar Mudstone Formation (RMF), Staithes Sandstone and Cleveland Ironstone Formation (SSF), and Whitby Mudstone Formation (WMF), which dip gently by a few degrees to the north (Figure 8a). Slope failure occurs within the WMF in the upper parts of the slope (more details can be found in Gunn *et al.* (2013), Merritt *et al.* (2014) and Uhlemann *et al.* (2015b)).

Permanently installed electrodes were deployed along 5 parallel lines running from the base to the top of the slope each with 32 electrodes spaced at intervals of 4.75 m

(measured along the ground surface) and with 9.5 m between the lines (Wilkinson *et al.* 2016). We show results from the western-most line, on which 516 measurements were made using the dipole-dipole array with  $a=4.75$  to 14.25 m and  $n=1$  to 8. The data were measured in reciprocal pairs and had very low levels of noise with 98% of the data exhibiting reciprocal errors below 0.5% (Wilkinson *et al.* 2010). The data set measured on 6th March 2008 is used as the base data set. The positions of the electrodes had also been measured on this date (although direct measurements of the electrode positions were made much less frequently than the geoelectrical measurements, see Uhlemann *et al.* (2015a)). Figure 8a shows the inverse model for this data set with the main geological formations marked. The L-curve method (Farquharson and Oldenburg 2004; Loke *et al.* 2014) is used to estimate the appropriate damping factor  $\lambda$ . The data set measured on 31st March 2009 is used as the test data set. The positions of the electrodes that had moved were also directly re-measured on this date, thereby providing a means to test the accuracy of the inversion procedure.

Figure 8b shows the apparent resistivity pseudosection and inverse model for the 2009 data set using the positions of the electrodes from the 2008 survey (i.e. assuming no movement of the electrodes). The 2009 inverse model has a significantly higher data misfit of 1.5% compared to 0.6% for the 2008 model (Figure 8a). A comparison of the measured electrode positions shows the largest movements occurred at electrodes number 9 (1.56 m shift), 10 (1.03 m), 11 (0.71 m) and 12 (0.53 m) down the slope. The apparent resistivity pseudosection and model both show significant distortions in the vicinity of these electrodes (Figure 8b). The RMS difference between the measured electrode positions from the 2008 and 2009 surveys is 0.37 m (Table 3).

Figure 9a shows the inverse model obtained when the electrodes are allowed to shift. A value of 3.0 is used for the relative damping factor  $\alpha$  and the inverse model from the 2008 survey (Figure 8a) is used as the starting model. The distortions in the model near electrode 9

are removed and a lower misfit of 0.6% is obtained. It also has a significantly lower RMS difference of 0.19 m (Table 3) between the measured electrode positions for the 2009 survey and the estimated positions from the inversion procedure. Figure 10a shows the positions of the electrodes measured in the 2008 and 2009 surveys as well as the estimated positions. The shift in the electrode positions is small over most of the profile except at electrodes 9 to 12. Figure 10b shows a more detailed plot of the section of the profile between electrodes 6 to 17 that shows the changes in the positions more clearly. The difference in the position of electrode 9 (Figure 10b) between 2008 (blue circle) and 2009 (black circle) surveys is reduced from 1.56 to 0.52 m by the inversion method (green rectangle). A closer examination of Figure 10b shows the inversion method produced a slight shift in the calculated positions of electrodes 15 to 17 up the slope by about 0.2 m. This is probably an artefact (possibly due to temporal changes in the resistivity) as it is expected that the movement of the electrodes (if any) will be down the slope based on the known geology and topography (Wilkinson *et al.* 2010; 2016). The inversion artefact does not have a significant effect of the results as it is only about 4% of the electrode spacing. However, the data set provides a test of a method to incorporate the expected direction of movement into the inversion method as a constraint to ensure changes in the electrode positions only occur down the slope. We use the method of transformations (Daniels 1978) to include the constraint. The variable for the horizontal position of an electrode,  $x_k$ , is replaced by a new variable,  $\tau_k$ , using the following equation.

$$x_k = x_{ku} - \tau_k^2 \quad (20)$$

$x_{ku}$  is the upper limit for  $k$ th the electrode position. If this is set at the position of the electrode from the 2008 survey, the transformation ensures that the new position of the electrode from the optimisation routine will be less than the original position (i.e. downslope). The required Jacobian values used in the optimisation routine are replaced as follows.

$$\frac{\partial \phi_i}{\partial \tau_k} = -2\tau_k \frac{\partial \phi_i}{\partial x_k} \quad (21)$$

Figure 9b shows the inverse model obtained with the additional constraint. The small up slope movements at electrodes 15 to 17 are eliminated (Figure 10b). The resistivity model is very similar to that obtained with unconstrained movement of the electrodes in Figure 9a. This is probably because the upwards shift at a few electrode positions from the unconstrained inversion is very small. However, adding the constraint does significantly reduce the RMS difference between calculated and measured electrode positions from 0.19 to 0.12 m (Table 3). This difference is only about 2.5% of the average distance between the electrodes. Finally, we show the model obtained when the measured positions of the electrodes from the 2009 survey are used for the inversion (Figure 9c). There are no significant differences between the three models shown in Figure 9. This shows that the technique used to estimate the positions of the electrodes from the resistivity data is sufficiently accurate.

## CONCLUSIONS

A fast technique to calculate the Jacobian matrix values for shifts in the electrode positions using the adjoint-equation method is presented. The use of the inverse model from the initial data set (with accurate electrode positions) as the starting model for the inversion of a later data set reduces the distortions in the surface topographic profile caused by subsurface resistivity variations, thereby giving more accurate calculated electrode positions. We also demonstrate the use of the method of transformations as a constraint in cases where it is known from geological and topographical information that the electrodes movement will be unidirectional. Tests with a field data set show that the average accuracy in the recovered electrode positions is better than 5%. The joint inversion of electrode displacement and

resistivity has the dual benefits minimising distortions in resistivity images due to electrode displacements and providing quantitative information with which to track landslide movement or other forms of ground instability.

Research is being carried out to apply the same techniques to detect changes in the electrode positions in 3-D surveys (Loke *et al.* 2016).

## **ACKNOWLEDGEMENTS**

The contributions of P.B. Wilkinson, J.E. Chambers and P. I. Meldrum to this paper are published with permission of the Executive Director of the British Geological Survey (NERC).



## REFERENCES

- Auken, E., Pellerin, L., Christensen, N. B., Sørensen, K. I. 2006, A survey of current trends in near-surface electrical and electromagnetic methods. *Geophysics* **71**, G249-G260
- Bing Z. and Greenhalgh S.A. 1999. Explicit expressions and numerical calculations for the Fréchet and second derivatives in 2.5D Helmholtz equation inversion. *Geophysical Prospecting* **47**, 443-468.
- deGroot-Hedlin C. and Constable S. 1990. Occam's inversion to generate smooth, two-dimensional models from magnetotelluric data. *Geophysics* **55**, 1613-1624.
- Chambers J.E., Wilkinson P.B., Kuras O., Ford J. R., Gunn D.A., Meldrum P. I., Pennington C.V.L., Weller A.L., Hobbs P.R.N., Ogilvy R.D. 2011. Three-dimensional geophysical anatomy of an active landslide in Lias Group mudrocks, Cleveland Basin, UK. *Geomorphology* **125**, 472-484
- Chambers J.E., Gunn D.A., Wilkinson P.B., Meldrum P.I., Haslam E., Holyoake S., Kirkham M., Kuras O., Merritt A. and Wragg J. 2014. 4D electrical resistivity tomography monitoring of soil moisture dynamics in an operational railway embankment. *Near Surface Geophysics* **12**, 61-72.
- Daniels R.W. 1978. *An introduction to numerical methods and optimization techniques*. Elsevier North-Holland.
- Dey A. and Morrison H.F. 1979. Resistivity modelling for arbitrary shaped two-dimensional structures. *Geophysical Prospecting* **27**, 106-136.
- Farquharson C.G. and Oldenburg D.W. 1998. Nonlinear inversion using general measures of data misfit and model structure. *Geophysical Journal International* **134**, 213-227.
- Farquharson C.G. and Oldenburg D.W. 2004. A comparison of automatic techniques for estimating the regularization parameter in non-linear inverse problems. *Geophysical Journal International* **156**, 411-425.

- Golub G. and van Loan C.F. 1996. *Matrix computations (Third Edition)*. The John Hopkins University Press.
- Gunn D.A., Chambers J.E., Hobbs P.R.N., Ford J.R., Wilkinson P.B., Jenkins G.O. and Merritt A. 2013. Rapid observations to guide the design of systems for long-term monitoring of a complex landslide in the Upper Lias clays of North Yorkshire, UK. *Quarterly Journal of Engineering Geology and Hydrogeology* **46**, 323-336.
- Jennings A. and McKeown J.J. 1992. *Matrix computation (Second edition)*. John Wiley and Sons Ltd.
- Kim J.H. 2014. Simultaneous Inversion of Resistivity Structure and Electrode Locations in ERT. 20th European Meeting of Environmental and Engineering Geophysics, Athens, Greece, 14-18 September 2014, We Olym 10.
- Li Y., and D. W. Oldenburg, 2000. 3-D inversion of induced polarization data. *Geophysics* **65**, 1931-1945.
- Loke M.H. and Barker R.D. 1996. Rapid least-squares inversion of apparent resistivity pseudosections by a quasi-Newton method. *Geophysical Prospecting* **44**, 131-152.
- Loke M.H. 2000. Topographic modelling in resistivity imaging inversion. 62nd EAGE Conference & Technical Exhibition, Extended Abstracts, D-2.
- Loke M.H., Acworth I. and Dahlin T. 2003. A comparison of smooth and blocky inversion methods in 2D electrical imaging surveys. *Exploration Geophysics* **34**, 182-187.
- Loke M.H. and Dahlin T. 2010. Methods to reduce banding effects in 3-D resistivity inversion. Near Surface 2010, Zurich, Switzerland, Expanded Abstracts, A16.
- Loke M.H., Chambers J.E., Rucker D.F., Kuras O. and Wilkinson P.B. 2013. Recent developments in the direct-current geoelectrical imaging method. *Journal of Applied Geophysics* **95**, 135-156.

- Loke M.H., Dahlin T. and Rucker D.F. 2014. Smoothness-constrained time-lapse inversion of data from 3-D resistivity surveys. *Near Surface Geophysics* **12**, 5-24.
- Loke M.H., Wilkinson P.B. and Chambers J.E. 2016. 3-D resistivity inversion with electrodes displacements. ASEG-PESA-AIG 25th Geophysical Conference and Exhibition, August 21–24, 2016, Adelaide, Australia, Extended Abstracts, 809-813.
- McGillivray P.R. and Oldenburg D.W. 1990. Methods for calculating fréchet derivatives and sensitivities for the non-linear inverse problem : a comparative study. *Geophysical Prospecting* **38**,499-524.
- Merritt A.J., Chambers J.E., Murphy W., Wilkinson P.B., West L.J., Gunn D.A., Meldrum P.I., Kirkham M. and Dixon N. 2014. 3D ground model development for an active landslide in Lias mudrocks using geophysical, remote sensing and geotechnical methods. *Landslides* **11**, 537-550
- Oldenburg D.W and Li Y. 1994. Inversion of induced polarization data. *Geophysics* **59**, 1327-1341.
- Press W.H., Teukolsky S.A., Vetterling W.T. and Flannery B.P. 1992. *Numerical Recipes in C (Second Edition)*. Cambridge University Press.
- Queralt P., Pous J. and Marcuello A. 1991. 2-D resistivity modeling: An approach to arrays parallel to the strike direction. *Geophysics* **56**, 941-950.
- Sasaki Y. 1989, Two-dimensional joint inversion of magnetotelluric and dipole-dipole resistivity data. *Geophysics* **54**, 254-262.
- Sasaki Y. 1994. 3-D resistivity inversion using the finite element method. *Geophysics* **59**, 1839–1848.
- Seaton W.J. and Burbey T.J. 2000. Aquifer characterization in the Blue Ridge physiographic province using resistivity profiling and borehole geophysics : Geologic analysis. *Journal of Environmental & Engineering Geophysics* **5**(3), 45-58.

- Schwarz H.R., Rutishauser H. and Stiefel E., 1973. *Numerical analysis of symmetric matrices*. Prentice-Hall, Inc.
- Silvester P.P. and Ferrari R.L. 1990. *Finite elements for electrical engineers (2nd. ed.)*. Cambridge University Press.
- Supper R., Ottowitz D., Jochum B., Römer A., Pfeiler S., Kauer S., Keuschnig M. and Ita A. 2014a. Geoelectrical monitoring of frozen ground and permafrost in alpine areas: field studies and considerations towards an improved measuring technology. *Near Surface Geophysics* **12**, 93-115.
- Supper R., Ottowitz D., Jochum B., Kim J.H., Römer A., Baron I., Pfeiler S., Lovisolo M., Gruber S. and Vecchiotti F. 2014b. Geoelectrical monitoring: An innovative method to supplement landslide surveillance and early warning. *Near Surface Geophysics* **12**, 133-150.
- Uhlemann S., Wilkinson P.B., Chambers J.E., Maurer H., Merritt A.J., Gunn D.A. and Meldrum P.I. 2015a. Interpolation of landslide movements to improve the accuracy of 4D geoelectrical monitoring. *Journal of Applied Geophysics* **121**, 93-105.
- Uhlemann S., Smith A., Chambers J.E., Dixon N., Dijkstra T., Haslam E., Meldrum P.I., Merritt A.J., Gunn D.A. and Mackay J. 2015b. Assessment of ground-based monitoring techniques applied to landslide investigations. *Geomorphology* **253**, 438-451.
- Wilkinson P.B., Chambers J.E., Meldrum P.I., Gunn D.A., Ogilvy R.D. and Kuras O. 2010. Predicting the movements of permanently installed electrodes on an active landslide using time-lapse geoelectrical resistivity data only. *Geophysical Journal International* **183**, 543-556.
- Wilkinson P.B., Uhlemann S., Chambers J.C., Meldrum P.I. and Loke M.H. 2015a. Development and testing of displacement inversion to track electrode movements on

- 3D Electrical Resistivity Tomography monitoring grids. *Geophysical Journal International* **200**, 1566-1581.
- Wilkinson P.B., Uhlemann S., Meldrum P.I., Chambers J.C., Carrière S., Oxby L.S. and Loke M.H. 2015b. Adaptive time-lapse optimized survey design for electrical resistivity tomography monitoring. *Geophysical Journal International* **203**, 755-766.
- Wilkinson P.B., Chambers J.E., Uhlemann S., Meldrum P.I., Smith A., Dixon N. and Loke M.H. 2016. Reconstruction of landslide movements by inversion of 4-D electrical resistivity tomography monitoring data. *Geophysical Research Letters* **43**, 1166-1174.
- Xu S.Z., Duan B.C. and Zhang D.H. 2000. Selection of the wavenumbers  $k$  using an optimization method for the inverse Fourier transform in 2.5-D electrical modeling. *Geophysical Prospecting* **48**, 789-796.
- Zhou B. and Dahlin T. 2003. Properties and effects of measurement errors on 2D resistivity imaging surveying. *Near Surface Geophysics* **1**, 105-117.

## List of figure captions

Figure 1. (a) Quadrilateral element used in the finite-element method. (b) Finite-element mesh with 6 nodes in the horizontal direction and 5 nodes in the vertical direction. The node numbers are shown. (c) Schematic diagram of the structure of the capacitance matrix equation showing the non-zero elements. D represent a diagonal element while X represents a non-zero off-diagonal element. The section of the  $\frac{\partial \mathbf{C}}{\partial z_k}$  matrix that has non-zero elements due to a shift of an electrode is marked in red.

Figure 2. Part of 2-D finite-element mesh used. Only the nodes that lie between electrodes 2 and 4 are affected by a shift in the position of electrode 3.

Figure 3. Effects of different changes in electrode position or subsurface resistivity. (a) to (c) show the effect of a shift of 0.1 m in different directions of the electrode at the 10 m mark on the measured apparent resistivity values for a homogeneous half-space of 100  $\Omega\text{m}$ . (d) and (e) show the effect of a 10% increase or decrease in the resistivity of a 1 square meter block directly below the electrode at the 10 m mark. The dipole-dipole measurements have  $a=1$  m and  $n=1$  to 10.

Figure 4. (a) The synthetic model for the initial time-lapse data set with equally spaced electrodes, together with the apparent resistivity pseudosection and inversion model. (b) The perturbed synthetic model with the electrode originally at the 5 m mark shifted horizontally by 0.3 m, and the electrode at the 17 m mark shifted upwards by 0.4 m. The thickness of the 20  $\Omega\text{m}$  prism below the 8 m mark is increased and a new 70  $\Omega\text{m}$  prism is added below the 13

m mark. The resulting inversion model using incorrect (i.e. fixed equally spaced) electrode positions is shown.

Figure 5. The inverse models for the second time-lapse data set using different relative damping factors for the  $x$  and  $z$  coordinates of the electrodes. A homogeneous half-space is used as the starting resistivity model. The electrodes are equally spaced and on a flat surface in the starting model but are allowed to change in the optimisation routine.

Figure 6. The surface elevation profiles from the coordinates of the electrodes obtained by the inversion of the data set using (a) a homogeneous half-space as the starting model, (b) using the model obtained from the inversion of the initial time-lapse data set as the starting model. A vertical exaggeration of 10 times is used in this plot.

Figure 7. The inverse models for the second time-lapse data set using different relative damping factors for the  $x$  and  $z$  coordinates of the electrodes. The model obtained from the inversion of the first time-lapse data set is used as the starting resistivity model.

Figure 8. (a) Inverse model for Hollin Hill survey data set measured on 6th March 2008. The inferred boundaries between the Whitby (WMF), Staithes and Cleveland (SSF) and Redcar (RMF) formations are marked by dotted black lines. (b) Inverse model for the 31st March 2009 data using the 2008 electrode positions.

Figure 9. Inverse models for Hollin Hill survey 2009 data set using (a) variable electrode positions, and (b) with an additional downwards movement constraint, and (c) directly measured electrode positions.

Figure 10. (a) Plot of the electrode positions along the entire survey line. (b) Close up of section of the surface profile with the largest movement of electrodes.



## List of table captions

Table 1. Effects of different changes on the apparent resistivity values measured with the dipole-dipole array over a half-space of 100  $\Omega\text{m}$ . The minimum and maximum apparent resistivity values (and the range) are listed.

Table 2. Results from the inversion of the synthetic data set using different electrode shift relative damping factors and starting models.  $\alpha$  = Relative damping factor.  $g$  = data misfit (%).  $S_r$  = normalized RMS difference between true and calculated electrode positions.  $R_r$  = RMS difference between logarithms of inversion model cell resistivity values and actual model.  $S_A$  = Combined positions and resistivity misfits =  $S_r + R_r$ .

Table 3. Results using different inversion methods for the Hollin Hill field data set.  $g$  = data misfit (%).  $S_r$  = normalized RMS difference between true and calculated electrode positions (the misfit in meters is shown in brackets).

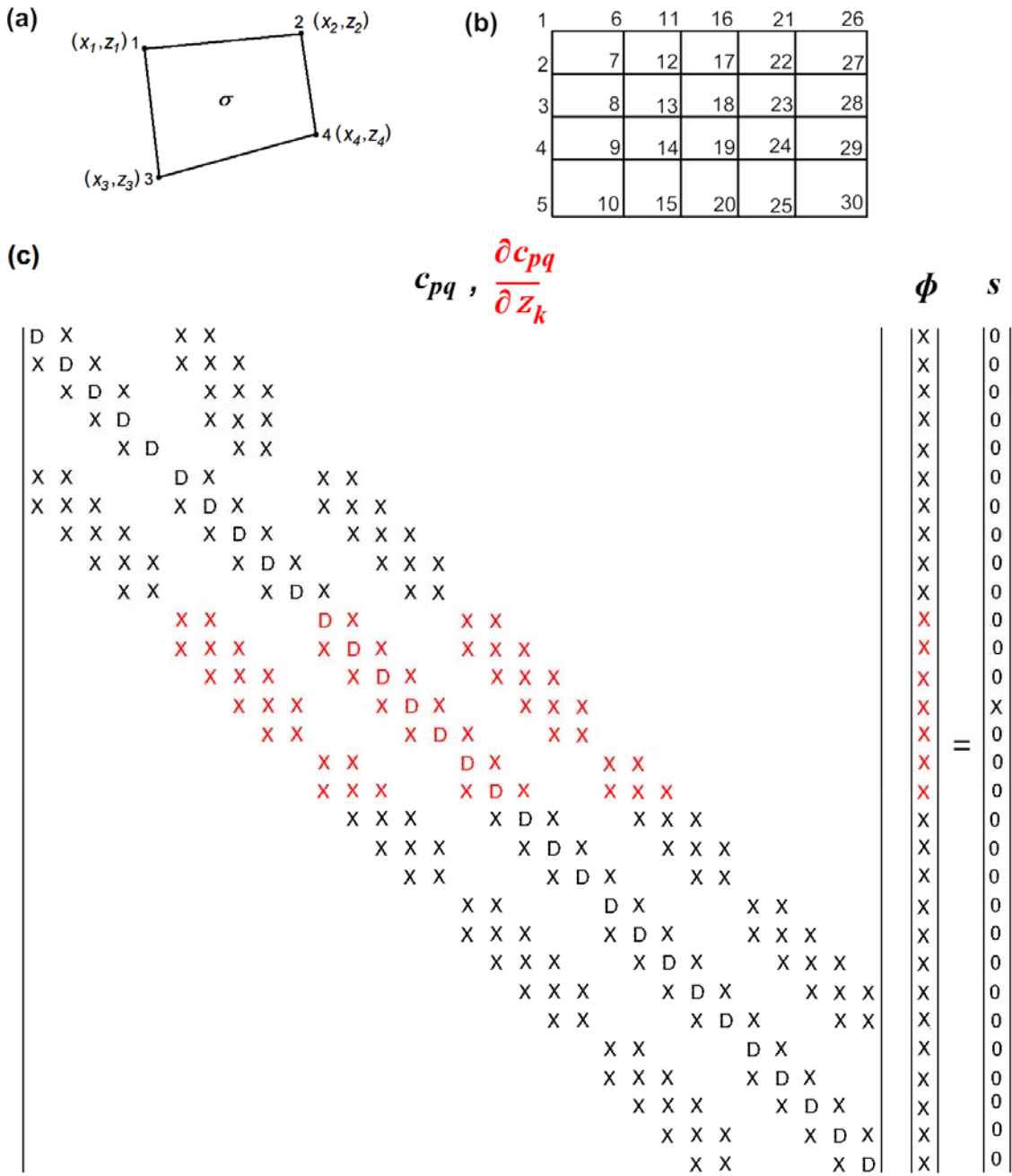


Figure 1. (a) Quadrilateral element used in the finite-element method. (b) Finite-element mesh with 6 nodes in the horizontal direction and 5 nodes in the vertical direction. The node numbers are shown. (c) Schematic diagram of the structure of the capacitance matrix equation showing the non-zero elements. D represent a diagonal element while X represents a non-zero off-diagonal element. The section of the  $\frac{\partial C}{\partial z_k}$  matrix that has non-zero elements due to a shift of an electrode is marked in red.

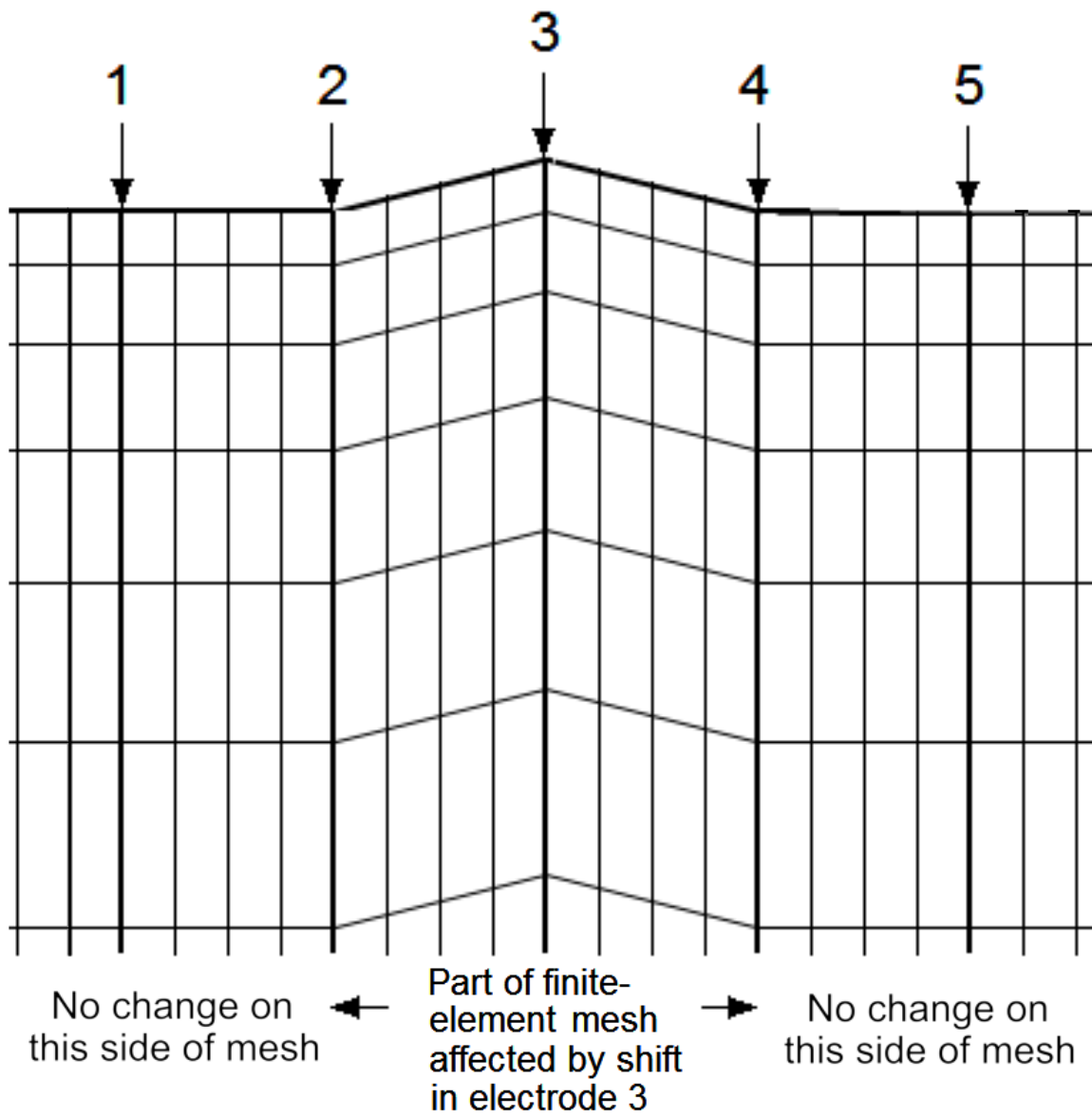


Figure 2. Part of 2-D finite-element mesh used. Only the nodes that lie between electrodes 2 and 4 are affected by a shift in the position of electrode 3.

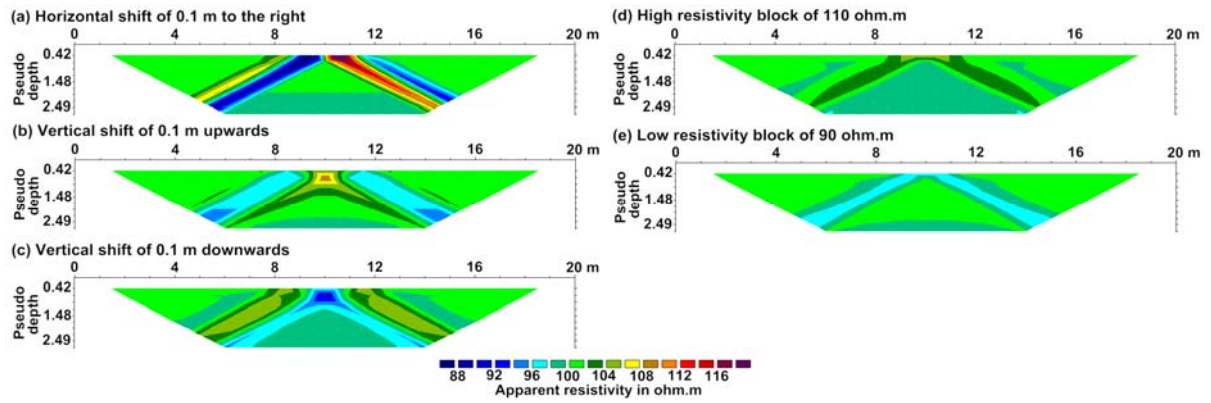


Figure 3. Effects of different changes in electrode position or subsurface resistivity. (a) to (c) show the effect of a shift of 0.1 m in different directions of the electrode at the 10 m mark on the measured apparent resistivity values for a homogeneous half-space of 100  $\Omega\text{m}$ . (d) and (e) show the effect of a 10% increase or decrease in the resistivity of a 1 square meter block directly below the electrode at the 10 m mark. The dipole-dipole measurements have  $a=1$  m and  $n=1$  to 10.

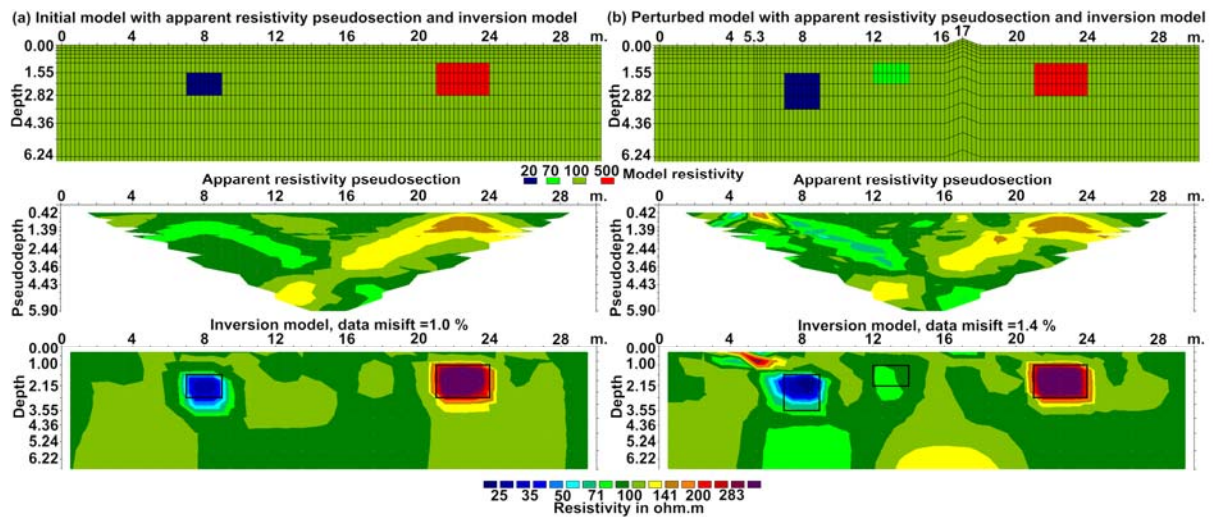


Figure 4. (a) The synthetic model for the initial time-lapse data set with equally spaced electrodes, together with the apparent resistivity pseudosection and inversion model. (b) The perturbed synthetic model with the electrode originally at the 5 m mark shifted horizontally by 0.3 m, and the electrode at the 17 m mark shifted upwards by 0.4 m. The thickness of the 20  $\Omega$ m prism below the 8 m mark is increased and a new 70  $\Omega$ m prism is added below the 13 m mark. The resulting inversion model using incorrect (i.e. fixed equally spaced) electrode positions is shown.

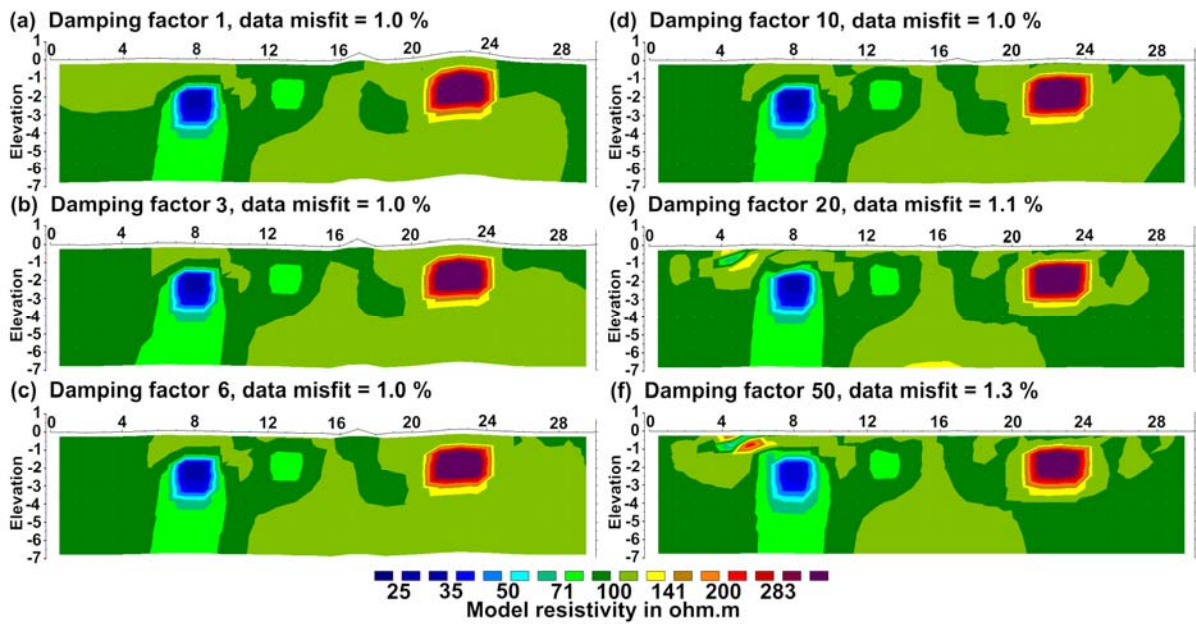


Figure 5. The inverse models for the second time-lapse data set using different relative damping factors for the  $x$  and  $z$  coordinates of the electrodes. A homogeneous half-space is used as the starting resistivity model. The electrodes are equally spaced and on a flat surface in the starting model but are allowed to change in the optimisation routine.

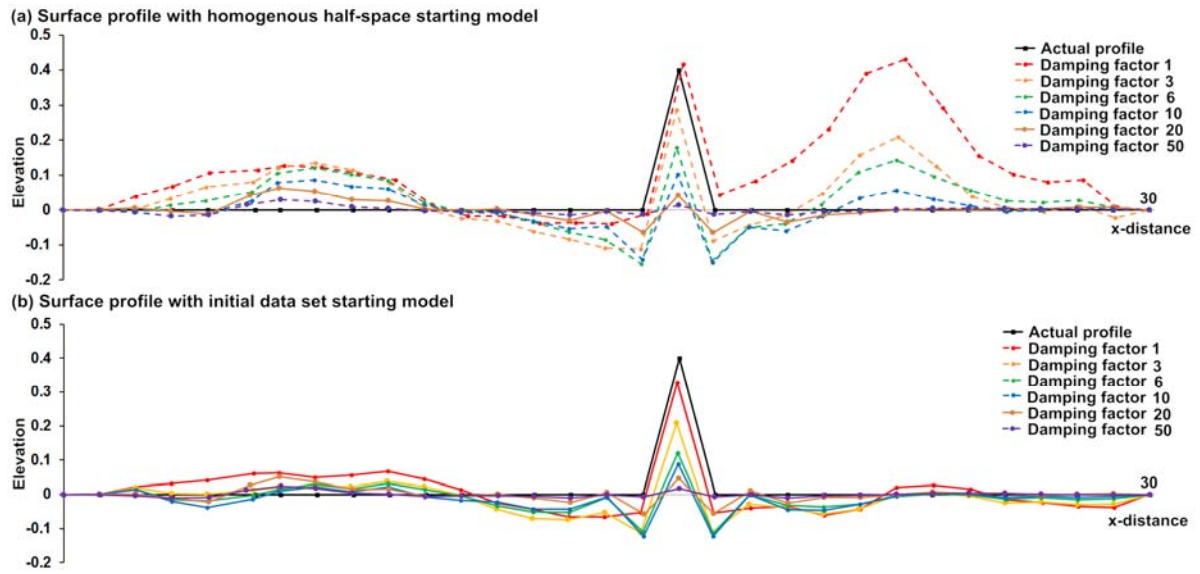


Figure 6. The surface elevation profiles from the coordinates of the electrodes obtained by the inversion of the data set using (a) a homogeneous half-space as the starting model, (b) using the model obtained from the inversion of the initial time-lapse data set as the starting model. A vertical exaggeration of 10 times is used in this plot.

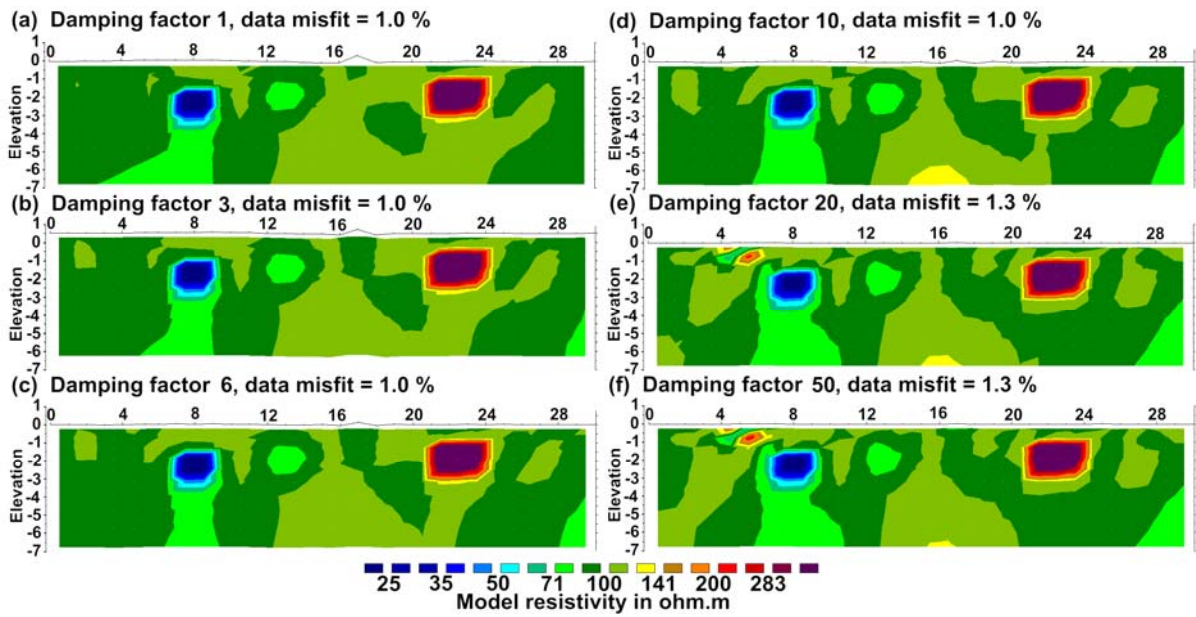


Figure 7. The inverse models for the second time-lapse data set using different relative damping factors for the  $x$  and  $z$  coordinates of the electrodes. The model obtained from the inversion of the first time-lapse data set is used as the starting resistivity model.



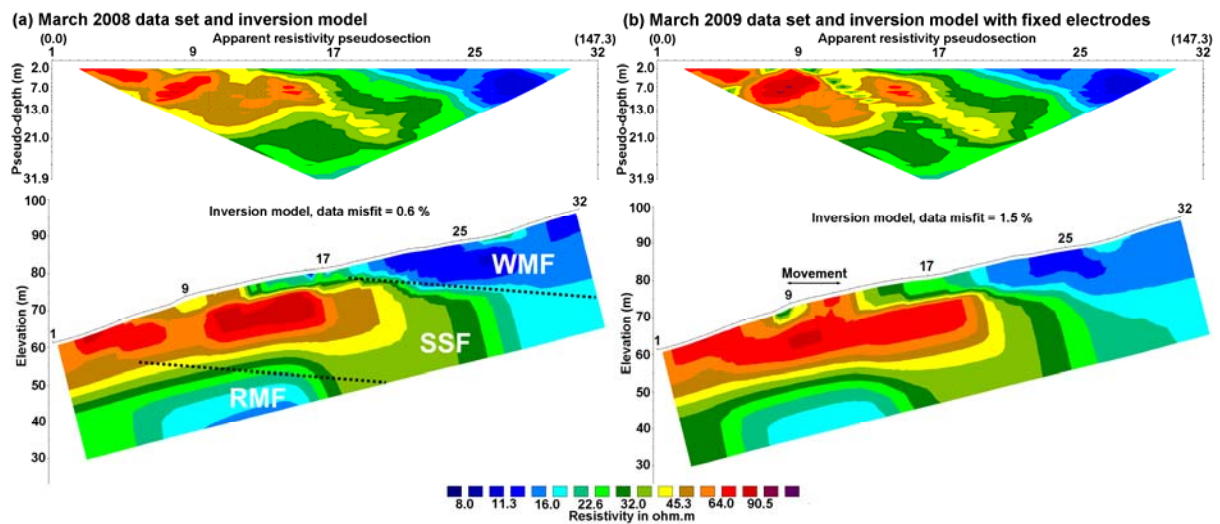


Figure 8. (a) Inverse model for Hollin Hill survey data set measured on 6th March 2008. The inferred boundaries between the Whitby (WMF), Staithes and Cleveland (SSF) and Redcar (RMF) formations are marked by dotted black lines. (b) Inverse model for the 31st March 2009 data using the 2008 electrode positions.

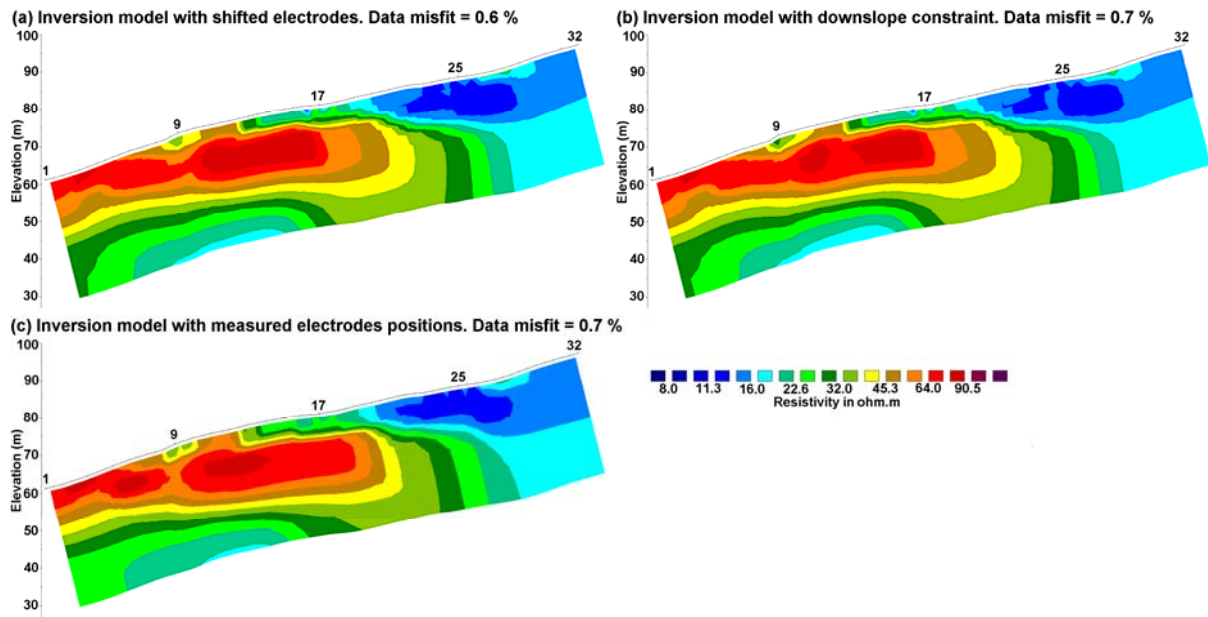
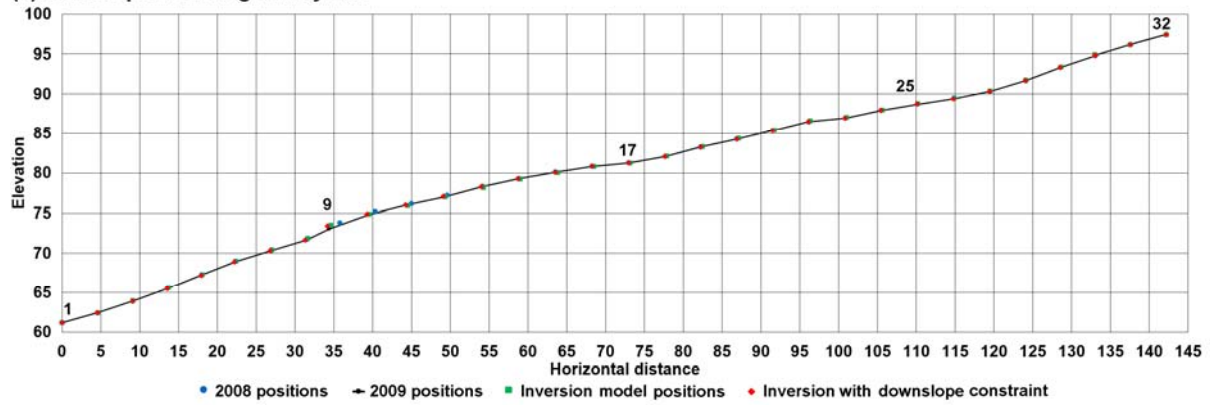


Figure 9. Inverse models for Hollin Hill survey 2009 data set using (a) variable electrode positions, and (b) with an additional downwards movement constraint, and (c) directly measured electrode positions.

(a) Surface profile along survey line



(b) Detailed surface profile between electrodes 6 and 17

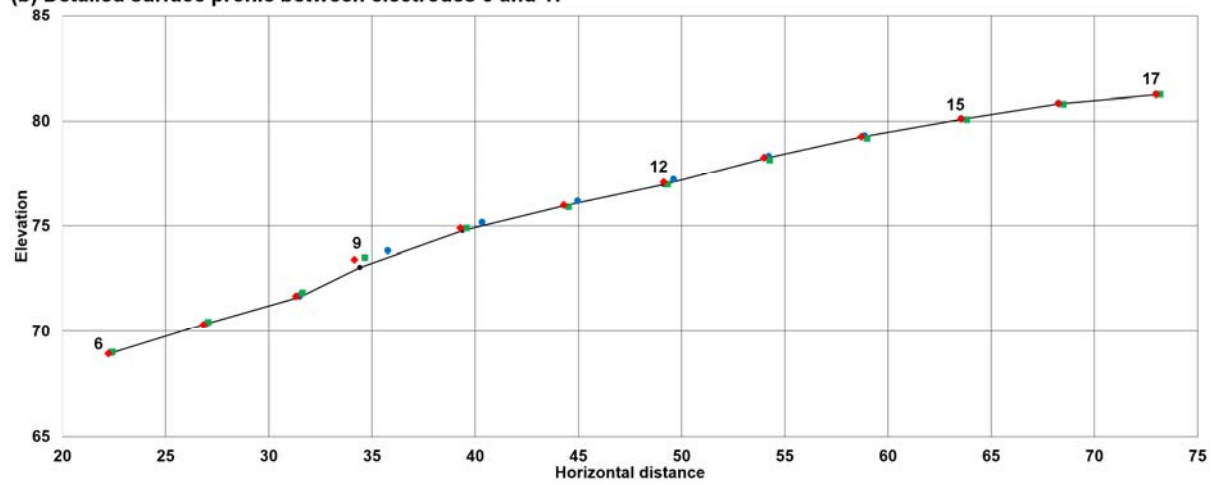


Figure 10. (a) Plot of the electrode positions along the entire survey line. (b) Close up of section of the surface profile with the largest movement of electrodes.

Table 1. Effects of different changes on the apparent resistivity values measured with the dipole-dipole array over a half-space of 100  $\Omega\text{m}$ . The minimum and maximum apparent resistivity values (and the range) are listed.

Type of change	Apparent resistivity values ( $\Omega\text{m}$ )
Horizontal shift of 0.1 m to the right	81 to 127 (46)
Vertical shift of 0.1 m upwards	95 to 110 (15)
Vertical shift of 0.1 m downwards	90 to 105 (15)
Increase in resistivity of block by 10%	98 to 106 (8)
Decrease in resistivity of block by 10%	96 to 102 (6)

Table 2. Results from the inversion of the synthetic data set using different electrode shift relative damping factors and starting models.  $\alpha$  = Relative damping factor.  $g$  = data misfit (%).  $S_r$  = normalized RMS difference between true and calculated electrode positions.  $R_r$  = RMS difference between logarithms of inversion model cell resistivity values and actual model.  $S_A$  = Combined positions and resistivity misfits =  $S_r + R_r$ .

Homogeneous half-space starting model				
$\alpha$	$g$	$S_r$	$R_r$	$S_A$
1	1.0	0.0350	0.0072	0.0422
3	1.0	0.0174	0.0071	0.0244
6	1.0	0.0172	0.0067	0.0239
10	1.0	0.0150	0.0064	0.0214
20	1.1	0.0139	0.0076	0.0215
50	1.3	0.0148	0.0097	0.0245
Initial time-lapse data set starting model				
$\alpha$	$g$	$S_r$	$R_r$	$S_A$
1	1.0	0.0103	0.0066	0.0169
3	1.0	0.0126	0.0065	0.0191
6	1.0	0.0125	0.0065	0.0190
10	1.0	0.0133	0.0070	0.0203
20	1.2	0.0133	0.0078	0.0211
50	1.3	0.0149	0.0090	0.0239

Table 3. Results using different inversion methods for the Hollin Hill field data set.  $g$  = data misfit (%).  $S_r$  = normalized RMS difference between true and calculated electrode positions (the misfit in meters is shown in brackets).

Inversion method	$g$	$S_r$
Fixed electrodes from 2008 survey	1.5	0.078 (0.37)
Electrodes allowed to shift	0.6	0.040 (0.19)
Down slope constraint used	0.7	0.025 (0.12)
Measured 2009 electrode positions	0.7	